Local Structural Characteristics of Pore Space in GDLs of PEM Fuel Cells Based on Geometric 3D Graphs

Ralf Thiedmann [1] Christoph Hartnig [2] Ingo Manke [3] Volker Schmidt [1]
Werner Lehnert [4] *

July 20, 2009

Abstract

Physical properties affecting transport processes inside the gas diffusion layer (GDL) in fuel cells mainly depend on the microscopic structure of its pore space. The presented characterization of the pore space is based on geometric 3D graphs, representing the complex microscopic structure. This description of the open volume contains the essential information on the geometrical structure of the pore space such as its connectivity. Additionally, the geometric structure of the graph, i.e., its vertices and edges, can be marked to display transport related properties such as pore diameters and pore necks. This 3D graph representation allows for an investigation of the local structural characteristics of the GDL by considering local tortuosity characteristics, pore sizes, and connectivity characteristics, respectively. The notion of a local shortest path length through the pore space of the GDL is introduced and the probability distribution of this random variable is computed. Its mean value is related to the (physical) tortuosity which is given by the

---

[*] Corresponding author: w.lehnert@fz-juelich.de; Electrochemical society active member

[1] Institute of Stochastics, Ulm University, 89069 Ulm, Germany

[2] Zentrum für Sonnenenergie– und Wasserstoff–Forschung Baden–Württemberg, 89081 Ulm, Germany
present address: BASF Fuel Cell GmbH, 65926 Frankfurt/Main, Germany

[3] Helmholtz-Zentrum Berlin für Energie und Materialien, 14109 Berlin, Germany

[4] Forschungszentrum Jülich GmbH, 52425 Jülich, Germany

ratio of the mean effective path length through the GDL and its thickness. This comprehensive information is used to distinguish the microstructures of different materials with equal (mean) porosities to serve as basis for further transport simulations. The proposed method for the construction of the 3D graph is based on 3D voxel data and can therefore be applied to simulated model data as well as to real (measured) 3D image data gained by means of, e.g., synchrotron tomography [1, 2]. The stochastic 3D model for the GDL considered in the present paper is an extended version of the multi–layer model introduced in [3] including a more flexible modeling of the binder. The dependence of the considered local characteristics of the entire GDL on the choice of the binder model has been demonstrated.

Keywords : Fuel Cell, Gas Diffusion Layer, Pore Space, 3D Graph, Tortuosity, Pore Size Distribution, Connectivity, Minimum Spanning Tree, Stochastic 3D Modeling, Multi–Layer Model

1 Introduction

Hydrogen can be used as an electrochemical energy storage and carrier which demands an effective way to convert hydrogen into electricity. A very promising way is the fuel cell technology due to its high efficiency, where a key component of PEM fuel cells is the gas diffusion layer (GDL) which is displayed in Figure 1. One of the main tasks of the GDL is the transportation of hydrogen and oxygen to the electrodes, where the electrochemical reaction takes place which produces electricity and water, see e.g. [4]. Thus, the drainage and storage of the produced water also belongs to the tasks of the GDL ensuring the right humidification of the electrode and the membrane: A dry membrane looses its conductivity, whereas excess water in the GDL and the electrode leads to flooding which stops the gas supply to the three phase boundary and therefore limits the current density.

For a better understanding of these physical processes within the GDL a detailed description especially of the open pore space is needed. In the present paper critical structural characteristics of the pore space are investigated where we do not restrict ourselves to standardized (mean) characteristics employed in physics and engineering but additionally compute the probability distributions of (local) structural characteristics as, e.g., tortuosity characteristics. The binary sample images required for these detailed computations are gained in two ways, by experimental measurements (synchrotron imaging) and from simulations based on stochastic modeling. In recent years, various modeling approaches for GDLs have been developed, see e.g. [3, 5, 6, 7, 8]. We will use an extended version of the multi–layer model introduced in [3]: hereby, the stochastic modeling of binder is made more flexible and different extents of the binder component can be taken into account; details are given in Section 4.2. The parameters of this model are fitted to the real (measured) structure of GDLs and local structural characteristics of the pore space are computed on this basis.

In the present approach, the pore space is described by a so-called geometric 3D graph that is, in a more pictorial way, a 3D skeleton of the pore space. Recently, various other attempts have been made to create networks describing the pore space, see e.g. [6, 9, 10, 11]. Such network representations have essential advantages in comparison with traditional modeling approaches of the pore space since they lead to important model reductions. Typically, the real 3D structure of the pore space is very complicated rendering direct numerical computations rather difficult. For example, grid–based computations require the description of the pore space by finite element methods (FEM). Numerical FEM computations on the other hand are rather time–consuming and often very restricted in the number of considered elements. Additionally, the results depend on the choice of the grid type and its resolution. The representation of the pore space by a geometric 3D graph however can simplify the computations drastically because the number of vertices and edges of such graphs (which can be interpreted as the pores and the connecting necks of the pore space) is much smaller compared to the number of elements used by a voxel representation. In addition, the dimension of the computation problem is reduced from 3D to 1D, because the edges of the graph are only 1D objects. Despite of this simplified representation of the pore space, the essential information on its geometrical structure as, for example, the connectivity is preserved. Furthermore, the vertices and edges of the graph are equipped with marks which can be taken to describe, e.g., the size of pores and necks at given locations. The additional information included in these weighted graphs is crucial for the investigation of transport, drainage and storage problems.

The weighted–graph representation of the pore space allows for the computation of physical characteristics of the open pore space of the GDL. An example of an important structural property besides the frequently mentioned porosity is the (mean) tortuosity which is usually defined as the ratio of the mean effective path length through a porous medium and the thickness of the medium ([12]).

An overview of theoretical and empirical porosity and tortuosity relations can be found in [13]. In the present paper, we introduce (uniquely defined) local structural characteristics describing tortuosity properties of porous media. They are based on shortest paths along the edges of the 3D graph representing the pore space. By using different weightings of the segments of these shortest paths the (local) effective path lengths can be approximated.

Furthermore, the 3D graph representation of the pore space enables one to introduce an object–based definition of pores and, in particular, pore centers by considering an appropriately chosen subset of vertices of the graph. Hence, for each pore, we can compute its size as well as its coordination number, i.e., the number of outgoing connections from a pore. By the computation of histograms, the probability distributions of these (local) structural characteristics can also be approximated. Further structural properties of the pore space can be investigated by means of the graph representation of the pore space, e.g., the so–called minimum spanning tree, which is a popular tool in graph theory.

The 3D computations for a synchrotron tomogram are performed on basis of a 3D image data set of the GDL as displayed in Figure 1 (b). In addition, we compare the results with synthetic model data which were obtained from stochastic simulations based on an extended version of the multi–layer model as introduced in [3]. This allows us to consider different scenarios for the modeling of binder and to show how the considered local characteristics of the entire GDL model depend on the specific choice of the binder model.

The paper is organized as follows: In Section 2 the representation of the pore space by means of geometric 3D graphs is described. Section 3 introduces the local structural characteristics considered in the present paper together with computation techniques. The stochastic multi–layer model introduced in [3] is briefly explained in Section 4. In particular, increased flexibility of the binder model is described. In Section 5 the numerical results of our computations are presented. A short discussion of the results is given in Section 6.

2 Graph Representation of Pore Space

The porosity of the GDL is the critical property which can be taken into account to describe the gas diffusion to the catalyst layer and the drainage of water produced within the electrochemical reaction. Typically, the pore space is described as a rather complex three dimensional structure. For any kind of computations a discretization is done, i.e., the pore space is investigated using finite element techniques, or, in other words, the pore space is subdivided into (many) small subsets. However, for efficient computations this representation is not very suitable due to the large number of elements which has to be considered. Therefore, we propose a representation of the complete pore space as one geometric 3D graph. Due to its construction, the main structural properties of the pore space such as the connectivity which assures the transport pathways are preserved. Such a graph only consists of one dimensional objects (line segments) which allows for efficient computations. Added marks on the vertices and edges of the graph (see Section 2.2) preserve the essential information on the pore space even in this easily trackable representation.

In the next section, the creation and treatment of the images is shortly explained.

2.1 Skeletonization of Binary 3D Images

A 3D image of (segmented) synchrotron data or simulated model data is normally given as a stack of 2D binary images, i.e., the 3D information is given as a 3D matrix with entries 0 or 1 representing occupied voxels (fibers) or empty space. To transform the voxel–given pore space into a graph, a skeletonization of the pore space is required. This means that voxels belonging to the pore space (foreground) are changed into background voxels in a way that the remaining (voxel–given) lines have a thickness of just one voxel, the connectivity, or *homotopy*, is thereby not changed. A 2D example is shown in Figure 2. Subpicture (a) shows two (material) objects, i.e., we are interested in the remaining white phases between these objects as our focus is set on the pore volume. Subpicture (b) contains the skeleton of the empty space, i.e., the pore space. The result of skeletonizing the pore space of the 3D multi–layer model is illustrated in Figure 3. For the skeletonization the algorithm described in [18] is used.

After skeletonization the pore space is represented by a skeleton of foreground voxels which has a thickness of just one voxel. A following classification of these voxels into *end voxels*, *line segment voxels*, and *junctions* is necessary. All foreground voxels with exactly one foreground neighbor are *end voxels.* All voxels with exactly two foreground neighbors are *line segment voxels*, and all voxels with more than two foreground neighbors are *junctions.* If such a junction consists of several voxels, the center of gravity is assumed to be the location of the junction. Then a 3D graph is constructed by connecting end voxels and junctions or end voxels and end voxels or junctions and junctions which are connected only via line segment voxels. A 2D example is shown in Figure 2 (c). If such a connection is not straight but curved, the connection is represented by a polygonal track instead of just one segment. Segments or polygonal tracks, respectively, can be marked in this procedure. A 3D graph representation of the pore space is shown in Figure 4.

2.2 Weighted Graph by Adding Marks

For a suitable representation of the pore space by a 3D graph marks which contain 3D information of the underlying pore space have to be considered additionally. These marks describe in a certain way the local capacity of the pore space. Therefore, each line segment of the graph is equipped with an additional information describing the radius of a ball that can be scrolled along it just touching the solid phase. In order to fix notation, we consider the 3D graph as a finite set of line segments $\ell_1, \ell_2, \ldots, \ell_m$, where $m \geq 1$ denotes the total number of segments of the graph. The radius of a ball that can be scrolled along a line segment l_n just touching the solid phase is denoted by $d_S(l_n)$.

An example in 2D is shown in Figure 5 (a). The distance value $d_S(\ell_n)$ is added as mark to the line segment ℓ_n of the graph representing the pore space. This marking is repeated for all segments $\ell_n, n = 1, \ldots, m$ which leads to a so–called weighted graph.

3 Local Structural Characteristics

In this section we introduce local structural characteristics of pore space which can be computed from 3D image data using the graph representation of the pore space as described in Section 2. By means of these structural characteristics we will analyze 3D data taken from the stochastic GDL model, which will be described in Section 4 below, as well as real (measured) 3D image data.

3.1 Shortest Path Length – A Local Tortuosity Characteristic

An important characteristic of porous media, which is considered when describing transport properties, is the porosity and in order to describe the pathway through different materials, their tortuosity. This physical characteristic is usually defined as the ratio of the mean effective path length through the pore space of a porous material and the material thickness, or, in other words, the extension of the real pathway compared to the minimum distance between the two points under consideration; the interested reader is refered to, e.g., [12, 13].

3.1.1 Effective Paths versus Shortest Paths

In literature, the tortuosity is usually described as a material constant, i.e., a single number representing a mean value. It can be shown (see [12, 14] and the references therein) that the effective path length does not only depend on the material itself, but also on environmental conditions of the experiment, e.g., temperature, pressure, and used gases. So the effective path length is not a uniquely defined material constant.

We introduce a (uniquely defined) local material characteristic which describes the notion of tortuosity in a slightly different way. It is related to 'real' physical tortuosity at a given location. Instead of the notion of the effective path through the material, we consider shortest paths. Moreover, we do not restrict ourselves to their mean value, as in the classical definitions of tortuosity, but consider the notion of shortest paths as a random variable. This allows us to determine the probability distribution of this random variable which contains much more structural information about the material than just a mean value. Furthermore, considering a certain weighted distribution of shortest paths where we additionally take the local capacity of pore space into account, see Section 3.2, we get an even better approximation of the effective path length.

3.1.2 Modeling of Starting Points

In order to compute shortest paths from top to bottom of the GDL along the edges of the 3D graph representing the pore space, we first have to determine the starting points of these paths. Therefore a two-dimensional Poisson point process with intensity $\lambda > 0$ is generated on the top (by definition) of the GDL. Such a point pattern follows the principle of complete spatial randomness (CSR, uniformly distributed points) and its intensity λ can be interpreted as the mean number of points per unit area.

This model for starting points of shortest paths is chosen based on the fact that gas molecules can start their diffusion or migration at any point of the GDL surface with the same probability (in ex situ experiments). Due to the spatial randomness, the specific choice of the intensity value λ of the underlying Poisson point process of starting points has practically no influence on the computed probability distribution of shortest path lengths, provided that the considered sample image or the number of realizations, respectively, is large enough.

3.1.3 Computation of Shortest Paths

For each randomly chosen starting point on the top the shortest path is computed from top to bottom along the edges of the 3D graph representing the pore space. The target location at the bottom is not considered any further. For the computation of shortest paths we use Dijkstra's algorithm, for details see, e.g., [26, 27].

3.2 Weighted Empirical Distributions of Shortest Path Length

In Section 3.1 we defined the starting points of shortest paths through the GDL using the CSR principle, where the notion of a shortest path was introduced in order to approximate the effective path length. The shortest path length can be seen as a mark of the corresponding starting point. Besides the shortest path length, we will flag each starting point with additional marks and, in this way, take into account different structural aspects of the GDL. These additional marks can be used for assigning individual weights to shortest paths according to their relevance, e.g., for transport processes. As a result we get a more realistic approximation of effective path lengths which is useful for an optimized approximation of 'real' tortuosity.

3.2.1 Weighting with Capacities

The individual weighting of shortest paths is an appropriate way to take the geometrical structure of the pore space into account in a more sophisticated way. For example, the weighting of shortest paths with their spherical distance to the fibers or binder as described in Section 2.2 can be used. This takes into account that paths through the GDL located in larger pores have a greater contribution to the overall transport ratio compared to paths located in smaller pores. Then, each shortest path is weighted with the maximum radius of a ball that can be scrolled along the shortest path from top to bottom just touching the solid phase, i.e., the fibers or binder, respectively.

3.2.2 Weighting with Voronoi–Area

As another additional mark component of the starting points, we can consider the area of the drainage basin around each starting point. The idea is that each shortest path is weighted according to the amount of material which should be transported along it to guarantee an evenly spread drainage at each location of the GDL. An example is shown in Figure 5 (b), where the (many) starting points on the left side generate small cells and the single point on the right side generate a large cell. Accordingly, the shortest path starting at the points on the left side get lower weights than the shortest path emanating from the point on the right.

We do this by using the Voronoi principle, i.e., the nearest neighborhood principle, on top of the GDL based on the starting points. Therefore the plane on top of the GDL is divided into convex polygons, where each convex polygon contains exactly one starting point, the so called nucleus. The polygon itself consists of all those points for which the corresponding starting point (nuclues) is the nearest neighbor among all starting points (nuclei). If the nuclei form a Poisson point process, as they do in our case and what can be seen in Figure 6 (a), the division of the plane is called Poisson–Voronoi tessellation, see [15, 16, 19] and Figure 6 (b). The area of the cell around a starting point is added as an additional mark to the corresponding shortest path.

By this kind of weighting, a measure for the amount of material (gas or water) is given which starts its way through the GDL at the corresponding nucleus of the Voronoi tessellation. Such a weighting also takes into account that paths through the GDL which start at similar locations are highly correlated, whereas paths emanating from starting points being far from each other can be assumed to be (more or less) independent.

3.3 Further Local Characteristics

Besides the tortuosity characteristic, described by a shortest–path approach given in Sections 3.1 and 3.2, further local structural characteristics can be considered using the 3D graph representation of the pore space.

3.3.1 Pore Size

The representation of the pore space by a geometric 3D graph enables the computation of pore sizes. The main problem in computing this characteristic for a material with a high porosity (about 80%) is the (unique) definition of pore centers. Using the 3D graph introduced in Section 2, we can consider all vertices of the 3D graph as potential pore centers. The pore size or pore radius is then the spherical distance of such a pore center to the solid phase, i.e., fibers or binder. If we took all vertices as pore centers, some pores would be contained partially or completely in other pores. Therefore only those vertices are considered as pore centers, which are not contained in larger pores, else the number of small pores would be overestimated.

Technically, the procedure to determine the pore size distribution can be described as follows: For each potential pore, i.e., vertex of the graph, the spherical distance to the solid phase is computed. This can be done very efficiently using a distance transformation as described e.g. in [21]. The pores are then ordered according to their pore radii, considering only the largest pore. All other pores with pore centers belonging to that pore, i.e., which centers are located in the largest pore, are not taken into account any further and deleted from the list of potential pore centers. Then, for the largest remaining (and not yet considered) pore the same procedure is realized, and so on. The result is a set of pores which can mutually overlap, but no pore contains a center of another pore. An example can be seen in Figure 7.

In subpicture a) all potential pores can be seen, i.e., each vertex is seen as a potential pore center and the balls around are the corresponding pores. In subpicture b) only the detected pores are shown.

Since we are mainly interested in the permeability of the GDL, we will only consider the (remaining) through–pores, i.e., pores with at least two outgoing throats. The (empirical) distribution of the radii of these pores can be seen as pore size distribution of the porous material under consideration.

The notion of pore size distribution is of special interest in chemical and engineering literature [22, 23]; characteristics of this type can be accessed directly from real GDLs by porosimetric methods such as mercury porosimetry or water porosimetry. However, in the present paper, the pore size distribution is computed according to the definition introduced above for different simulated model data as well as for synchrotron data, see Section 5.3. A comparison of our results with pore size distributions obtained by porosimetric methods is the subject of further investigations.

3.3.2 Coordination Number

Another important property is the connectivity of the pore space, see e.g. [22, 24] and references therein. A related local structural characteristic is the so–called coordination number (also called connectivity). It can be computed using the definition of pore centers introduced in Section 3.3.1 since it is the number of necks emanating from a pore. In our case, i.e., using the graph representation of the pore space introduced in Section 2, it is equal to the number of line segments emanating from a pore. This characteristic describes connectivity properties of porous materials and has been applied e.g. in geology [25].

3.3.3 Minimum Spanning Tree

A popular tool in graph theory, which can be used for describing connectivity properties of the pore space, is the so–called minimum spanning tree (MST). The basic idea is to remove as many edges as possible that all vertices which have been connected before are still connected. In other words, the MST is the graph with the same cluster properties (but different coordination numbers) as the original graph but with the minimum total edge length, where the total edge length is the sum of the lengths of all edges contained in the graph. For the computation of MST, Prim's algorithm is used, see e.g. [26, 27]. The MST is useful in order to investigate structural properties of the pore space of GDL, because the skeletonization algorithm considered in Section 2.1 preserves principale connectivity properties of the whole 3D pore space.

4 Stochastic Multi–Layer Model

In this section we briefly recall the stochastic 3D model developed in [3] which is used to generate simulated samples of GDL structures. Moreover, an extented version of binder modeling is proposed which is more flexible than the original binder model introduced in [3]. It allows us to consider different scenarios for the modeling of the binder and to show how the considered local characteristics of the entire GDL model depend on the specific choice of the binder model. Later on, in Section 5, the results of our computations for the local structural characteristics introduced in Section 3 are presented and compared for different scenarios of binder modeling.

4.1 Model for the Fibers

The multi–layer model considered is based on tools from stochastic geometry. The basic modeling component is a Poisson line tessellation (PLT) in the plane. A line tessellation, see Figure 8 (a), is a division of the plane into convex polytopes $\xi_1, \xi_2, \ldots$ which arise from randomly scattered lines $\ell_1, \ell_2, \ldots$ in the plane. A line ℓ_n in the plane can be described by its normal form, i.e., its (signed) orthogonal distance x_n to the origin and its direction m_n; see Figure 8 (b). In case of a PLT, the distances to the origin are modeled by a (one-dimensional) Poisson point process $(X_n)_{n\geq 1}$ on the real axis. Such a process is completely specified by its intensity $\gamma > 0$, where γ is the mean number of points per unit length. The direction of a line ℓ_n is modeled by a random variable M_n which is uniformly distributed in $(0, \pi]$ and independent from $(X_n)_{n\geq 1}$ as well as from M_m $\forall m \neq n$. In other words, the lines of a PLT can be seen as an independently marked Poisson process $(X_1, M_1), (X_2, M_2), \ldots$ with intensity $\gamma > 0$. A PLT with intensity $\gamma > 0$ is then the sequence $\Xi_1, \Xi_2, \ldots$ of (convex) random polytopes created by the intersecting random lines $(X_1, M_1), (X_2, M_2), \ldots$, where the Poisson process $X_1, X_2, \ldots$ has the intensity γ. For a PLT, the intensity γ can be interpreted as the mean total edge length per unit area. A realization of a PLT, i.e., the sequence $\xi_1, \xi_2, \ldots$, is shown in Figure 8 (a). Further details on random tessellations can be found e.g. in [15, 16].

So far, the PLT is described only in the plane, i.e., the lines of the PLT are 1D objects. To create 3D objects the lines are 'blown up', or more formally, they are dilated with respect to 3D. A dilation of a set $A \subset \mathbb{R}^3$ with a set $C \subset \mathbb{R}^3$ is mathematically described by the *Minkowski sum* $A \oplus C$ of A and C, where $A \oplus C = \{a + c : a \in A, c \in C\}$; see e.g. [17] for more details.

In order to model a single thin section of fibers, the edge set $\bigcup_{n=1}^{\infty} \partial\Xi_n$ of the underlying

PLT $(\Xi_n)_{n\geq 1}$ is dilated with respect to 3D, i.e., the Minkowski sum

$$\Big(\bigcup_{n=1}^{\infty} \partial\Xi_n\Big) \oplus C_{r_F} = \bigcup_{n=1}^{\infty} (\partial\Xi_n \oplus C_{r_F}) \tag{4.1}$$

is considered for e.g. a cube $C_{r_F} \subset \mathbb{R}^3$ with side length $2r_F > 0$ and centered at the origin. This leads to an object in 3D. The whole 3D fiber model consists of a stack of such dilated PLTs, where adjacent layers do just touch each other.

In the proposed multi–layer model, the 3D dilated PLTs representing the individual thin sections are assumed to be independent and identically distributed.

4.2 Models for the Binder

The binder is modeled by a so–called Bernoulli filling, where in each layer the cells of the dilated PLT containing binder are chosen at random with a certain probability $p > 0$. The filling of a cell is independent of the filling of other cells. An example is shown in Figure 9, where (a) shows the fiber system without binder and (b) the fiber system with a cell completely filled with binder. A 3D realization of the stochastic multi–layer model including binder is shown in Figure 10 (a).

However, the results of our computations presented in Section 5 show that the blocking effect for this kind of binder modeling is too strong compared to synchrotron image data of real GDLs. Therefore we propose a modified approach to binder modeling. The idea is that the cells are not necessarily filled completely but only to a certain extend. This partial filling of a cell chosen at random can be realized as follows. With a certain probability $p > 0$ a cell is chosen to contain binder, where the cells containing binder are chosen independently from each other. Then the segments forming the boundary of the cell, i.e., the lines of the basic PLT, are 'blown up' towards the interior of the cell to be filled (at least partly).

More precisely, the segments are dilated by a cube, centered at the origin with side length $2r_B > 2r_F > 0$, where only the part within the chosen cell is taken into account.

More formally, it holds that the binder B_n in a (chosen) cell Ξ_n is given by

$$B_n = ((\partial\Xi_n \oplus C_{r_B}) \setminus (\partial\Xi_n \oplus C_{r_F})) \cap conv(\partial\Xi_n \oplus C_{r_F})\,,$$

where $\partial\Xi_n$ denotes the boundary of Ξ_n and $conv(\partial\Xi_n \oplus C_{r_F})$ the convex hull of the dilated boundary of Ξ_n. An example in 2D is shown in Figure 9 (c). A realization of the 3D model can be seen in Figure 10 (b).

Note that the binder model, which has been introduced in [3], is contained as a special case for $r_B = \infty$.

4.3 Model Fitting

The extended binder model considered in Section 4.2 leads to the following formula for the expected volume fraction of binder $V_{binder}(\gamma, p, r_F, r_B)$, now depending on four parameters. It can be shown that the expected volume fraction of binder is equal to the probability that the origin belongs to binder. Thus, we have that

$$V_{binder}(\gamma, p, r_F, r_B) = p\Big(exp(-2\gamma r_F) - exp(-2\gamma r_B)\Big)\,, \tag{4.2}$$

where γ denotes the intensity of the PLT, $p > 0$ the probability that a cell contains binder, r_F the dilation parameter of the fibers, and r_B the dilation parameter of the binder. For fitting the model to data, we fit the expected porosity ε of the model to the porosity of real 3D data which is estimated as 0.78 (see [3]). To keep this value constant, the number of cells containing binder increases for decreasing values of r_B. Furthermore, the expected volume fraction of fibers in the 3D model is given by

$$V_{fiber}(\gamma, r_F) = 1 - \exp(-2\gamma r_F)\,,$$

where the following relationship holds

$$\varepsilon = 1 - \left(V_{fiber}(\gamma, r_F) + V_{binder}(\gamma, p, r_F, r_B)\right) .$$

In this relationship, we can plug in the known values of $\gamma = 0.025$, $r_F = 7.5/2\,\mu m$ and $\varepsilon = 0.78$ (see [3]). If we fix e.g. the value of r_B, then p is completely determined and we have fitted the model to real image data.

5 Numerical Results

In this section, the results of our numerical computations are presented, which have been performed for the local structural characteristics of the pore space introduced in Section 3.

5.1 Description of Image Data

The computations are done using simulated realizations of the stochastic multi–layer model for the GDL described in Section 4. The parameter values for the fiber modeling are $\gamma = 0.025$ and $r_F = 3.75\mu m$. Furthermore due to the resolution of the synchrotron data we use a quadratic profile of the fibers as described in [3].

To investigate the influence of the binder on structural properties of the GDL we model the binder in different ways. The first approach is a complete cell filling, i.e., $r_B = \infty$, as described in [3] with a filling probability of $p = 0.059$. Additionally we use the modeling approach introduced in Section 4.2 where the cells are filled with binder only partially. We do the computations for the three parameter combinations $r_B = 30$ and $p = 0.081$, $r_B = 18$ and $p = 0.116$, and $r_B = 6$ and $p = 0.555$, respectively. All four parameter combinations lead to a mean (total) porosity of $\varepsilon = 78\%$, see also Table 1.

The results are compared with the results from a 3D image data set, see Figure 1 (b), of a GDL which is gained by means of synchrotron tomography at Bessy [1, 2]. The preprocessing of this data set is done in the same way as described in [3] using a threshold and a subsequent opening. This data set has a voxel resolution of $1.5\,\mu m$. Thus, we use the same voxel resolution of $1.5\,\mu m$ for the realizations of the multi–layer model. Notice that the estimated porosity of the synchrotron data is 78%, too.

In order to keep the computational effort at a reasonable level, the realizations of our model are generated in a cuboid with $512 \times 512 \times 100$ voxels, which corresponds to $768\mu\mathrm{m} \times 768\mu\mathrm{m} \times 150\mu\mathrm{m}$, but several times. Due to the model construction, this leads to the same results than considering one huge simulated data set. The 3D data set gained from synchrotron tomography has a size of $1550 \times 1550 \times 1700$ voxels. Thus to get comparable results, we use a bootstrap (see e.g. [29]), i.e., we choose cuboids with $512 \times 512 \times 100$ voxels at random which are considered as samples from synchrotron data.

To reduce edge effects, we apply a minus sampling, i.e., we neglect data which are too close to the boundary of the sampling window.

5.2 Distribution of Tortuosity Characteristics

The principle idea is the estimation of the distribution of the shortest path length described in Section 3.1.3. The results for realizations of the stochastic multi–layer model for the GDL with different approaches to binder modeling can be seen in Figure 11. This figure also shows the result for the synchrotron data set. The mean values, which can be seen as an (rough) approximation of the (physical) tortuosity, and standard deviations are given in Table 2.

The (unweighted) shortest path approach, described above, is not an optimal description for the physical tortuosity. It does not take into account the pore and throat size. But for transportation processes through porous media, such capacities are important. Therefore the empirical distributions of the shortest paths are weighted with the spherical distances to the solid phase. The results for the different approaches to binder modeling and for the synchrotron data can be seen in Figure 12. The mean values, which can be seen as more realistic approximations of the physical tortuosity, and standard deviations are shown in Table 2.

The corresponding distributional results for area–weighting are shown in Figure 13. The mean values and standard deviations are given in Table 2.

The results presented in Table 2 clearly show that the choice of the binder model essentially influences the mean values and standard deviations of tortuosity characteristics. In particular, the binder model with complete cell filling has a too strong blocking effect compared to the synchrotron data. On the other hand, the binder model with partial filling of cells yields better fits. The same effect can be observed comparing the histograms shown in Figures 11 – 13. The histograms corresponding to complete filling of cells are too flat with rather heavy right tails, whereas the histograms computed for partial filling of cells and synchrotron data, respectively, have more similar shapes.

5.3 Pore Size Distribution

A further very important characteristic is the pore size distribution, where centers and sizes of the pores are defined as in Section 3.3.1. The results for the multi–layer model with its different approaches to binder modeling as well as for synchrotron data are shown in Figure 14. The mean values and standard deviations are given in Table 3.

The histograms computed from simulated data are slightly too flat compared to data from GDL, gained by means of synchrotron tomography. Therefore also the mean values differ.

This may be caused by the quite regularity of the simulated data compared to real measured 3D image data of GDL structures which may contain artefacts. A comparison of the here proposed method to determine a structural characteristic related to pore sizes with results from e.g. mercury porosimetry is the subject of further investigations. This comparison should also help to explain the differences in the results of pore sizes for simulated and real measured image data.

5.4 Distribution of Coordination Number

One possibility for describing the connectivity of the pore space is the computation of the coordination number, i.e., the number of throats emanating from a pore. The histograms of this structural characteristic for the different considered cases can be seen in Figure 15. The mean values and standard deviations are shown in Table 3.

Notice that in the results for the synchrotron data there are some pores with quite high coordination numbers (not shown in the histogram). They do not change the shape of the histogram significantly but increases the standard deviation. However, the mean values of the coordination number are quite similar for synchrotron data and simulated model data.

5.5 Connectivity of Pore Space — MST

For the connectivity of the pore space the minimum spanning tree, described in Section 3.3.3, can additionally be considered. The relative length of the MST, i.e., the ratio of the length of the MST and the length of the original graph delivers information about the connectivity of the pore space, additionally to the coordination number. In case that this ratio is equal to 1, the graph can not be shortened without loosing connectivity of the junctions or pores, respectively. If the ratio was equal to 0.5, half of the graph length could be removed but the connectivity would still be the same. The mean values of the relative length of MST are shown in Table 3. The standard deviation for the synchrotron data has not been addressed as due to the boot strap method, independent samples cannot be obtained. Therefore we only show the mean values for all considered data sets which are rather similar for synchrotron and simulated model data, respectively.

6 Summary and Conclusions

Local structural characteristics of the pore space of a GDL employed in PEM fuel cells are investigated. Therefore we introduce a graph representing the pore space. Based on the construction principles, the main structural properties are preserved. The procedure can be transfered to (model–based) simulated data sets as well as to real (experimentally measured) 3D image data. This graph representation offers great advantages. It enables the computation of several material–specific characteristics in a very efficient way where the usage of finite element methods can raise runtime and memory problems.

We introduce uniquely defined characteristics for describing tortuosity properties of porous media which are based on a shortest path approach. Considering these local structural characteristics we are even able to compute their empirical distribution functions. Obviously, they contain much more information than just mean values, used in the traditional definition of tortuosity. With respect to our local tortuosity characteristics, we clearly detect differences between various modeling scenarios for GDL structures, where only the binder model has been changed but the porosity remains the same. In particular, in order to get a better approximation of the physical tortuosity, different weightings for shortest paths are taken into account.

Furthermore, we introduce a unique definition of pore centers in porous media like the GDL of PEM fuel cells. This definition is not based on a global consideration of the porous medium but leads to an object–orientated notion of pores. Moreover, it allows the computation of pore sizes and their histograms as well as the computation of the coordination number of pores. The latter property describes the connectivity properties of the respective porous medium. Additionally, we investigate the connectivity of the pore space using a popular tool from graph theory, the minimum spanning tree.

The graph representation of the pore space which is based on given 3D structures of the fibers and binder allows for the computation of various local structural characteristics. In addition, it turns out that these characteristics contain comprehensive quantitative information to detect structural differences between materials of the same porosity.

Acknowledgements. This research has been supported by the German Federal Ministry for Education and Science (BMBF) under Grant No. 03SF0324A/C/E/F.

References

[1] I. Manke, Ch. Hartnig, M. Grünerbel, W. Lehnert, N. Kardjilov, A. Haibel, A. Hilger, J. Banhart (2007). Investigation of Water Evolution and Transport in Fuel Cells with High Resolution Synchrotron X–Ray Radiography. *Applied Physics Letters* **90**, 174105-1 – 174105-3.

[2] Ch. Hartnig, R. Kuhn, P. Krüger, I. Manke, N. Kardjilov, J. Goebbels, B.R. Müller, H. Riesemeier (2008). Water Management in Fuel Cells – A Challenge for Non–Destructive High Resolution Methods. *MP Materials Testing*, **50**, 609–614.

[3] R. Thiedmann, F. Fleischer, Ch. Hartnig, W. Lehnert, V. Schmidt (2008). Stochastic 3D-Modeling of the GDL Structure in PEM Fuel Cells Based on Thin Section Detection. *J. Electrochem. Soc.*, **155(4)**, B391 – B399.

[4] M.F. Mathias, J. Roth, J. Fleming, W. Lehnert (2003). Diffusion Media Materials and Characterisation. *Handbook of Fuel Cells, Volume III, Chapter 42, Ed. W. Vielstich, A. Lamm, H. Gasteiger.* J.Wiley & Sons, Chichester.

[5] V.P. Schulz, J. Becker, A. Wiegmann, P.P. Mukherjee, C.-Y. Wang (2007). Modeling of Two-Phase Behavior in the Gas Diffusion Medium of PEFCs via Full Morphology Approach. *J. Electrochem. Soc.* **154(4)**, B419–B426.

[6] G. Inoue, Y. Matsukuma, M. Minemoto (2007). Numerical Analysis of Two-Phase Transport in GDL of Polymer Electrolyte Fuel Cell. *Proceedings of the 2nd European Fuel Cell Technology and Applications Conference*, EFC2007-39024.

[7] M. Yoneda, M. Takimoto, S. Koshizuka (2007). Effects of Microstructure of Gas Diffusion Layer on Two-Phase Flow Transport Properties. *ECS Transactions*, **11**, 629–635.

[8] G. Inoue, T. Yoshimoto, Y. Matsukuma, M. Minemoto (2008). Development of Simulated Gas Diffusion Layer of Polymer Electrolyte Fuel Cells and Evaluation of its Structure. *Journal of Power Sources*, **175**, 145–158.

[9] P.K. Sinha, P.P. Mukherjee, C.-Y. Wang (2007). Impact of GDL Structure and Wettability on Water Management in Polymer Electrolyte Fuel Cells. *J. Mater. Chem.*, **17**, 3089–3103.

[10] J.T. Gostick, M.A. Ioannidis, M.W. Fowler, M.D. Pritzker (2007). Pore Network Modeling of Fibrous Gas Diffusion Layers for Polymer Electrolyte Membrane Fuel Cells. *Journal of Power Sources*, **173**, 277–290.

[11] P.K. Sinha, C.-Y. Wang (2007). Pore–Network Modeling of Liquid Water Transport in Gas Diffusion Layer of a Polymer Electrolyte Fuel Cell. *Electrochimica Acta*, **52**, 7936–7945.

[12] F. Keil (1999). *Diffusion und Chemische Reaktionen in der Gas/Feststoff–Katalyse.* Springer, Berlin.

[13] L. Shen, Z. Chen (2007). Critical Review of the Impact of Tortuosity on Diffusion. *Chem. Eng. Sci.*, **62**, 3748–3755.

[14] P. Asinari, M.C. Quaglia, M.R. von Spakovsky, B.V. Kasula (2007). Direct Numerical Calculation of the Kinematic Tortuosity of Reactive Mixture Flow in the Anode Layer of Solid Oxide Fuel Cells by the Lattice Boltzmann Method. *Journal of Power Sources*, **170**, 359–375.

[15] R. Schneider, W. Weil (2008). *Stochastic and Integral Geometry.* Springer, Berlin.

[16] D. Stoyan, W.S. Kendall, J. Mecke (1995). *Stochastic Geometry and its Applications.* 2nd ed. J. Wiley & Sons, Chichester.

[17] B. Jähne (2005). *Digital Image Processing.* 6th revised and extended ed., Springer, Berlin.

[18] C. Fourard, G. Malandain, S. Prohaska, M. Westerhoff (2006). Blockwise Processing Applied to Brain Microvascular Network Study. *IEEE Transactions on Medical Imaging* **25**, 1319–1328.

[19] A. Okabe, B. Boots, K. Sugihara, S.N. Chiu (2000). *Spatial Tessellations.* 2nd ed. J.Wiley & Sons, Chichester.

[20] J. Ohser, F. Mücklich (2000). *Statistical Analysis of Microstructures in Materials Science.* J. Wiley & Sons, Chichester.

[21] T. Saito, J.-I. Toriwaki (1994). New Algorithms for Euclidean Distance Transformations of an n-Dimensional Digitized Picture with Applications. *Pattern Recognition*, **27**, 1551–1565.

[22] G.S. Armatas (2006). Determination of the Effects of the Pore Size Distribution and Pore Connectivity Distribution on the Pore Tortuosity and Diffusive Transport in Model Porous Networks. *Chem. Eng. Sci.*, **61**, 4662–4675.

[23] P.H. Maheshwaria, R.B. Mathur, T.L. Dhamia (2008). The Influence of the Pore Size and its Distribution in a Carbon Paper Electrode on the Performance of a PEM Fuel Cell. *Electrochimica Acta* , **54**, 655–659.

[24] G.M. Laudone, G.P. Matthews, P.A.C. Gane (2008). Modelling Diffusion from Simulated Porous Structures. *Chem. Eng. Sci.*, **63**, 1987–1996

[25] M.J. Blunt, M.D. Jackson, M. Piri, P.H. Valvatne (2002). Detailed Physics, Predictive Capabilities and Macroscopic Consequences for Pore–Network Models of Multiphase Flow. *Adv. Water Resor*, **25**, 1069–1089.

[26] R. Diestel (2005). *Graph Theory.* Springer, Heidelberg.

[27] D. Jungnickel (1999). *Graphs, Networks and Algorithms.* Springer, Berlin.

[28] G. Casella, R.-L Berger (2002). *Statistical Inference.* 2nd ed. Duxbury, Pacific Grove (CA).

[29] S.N. Lahiri (2003). *Resampling Methods for Dependent Data.* Springer, New–York.

	p	ε
$r_B = 6$	0.555	78%
$r_B = 18$	0.116	78%
$r_B = 30$	0.081	78%
$r_B = \infty$	0.059	78%

Table 1: Parameter combinations for different approaches to binder modeling

Used data	Porosity	Shortest path length					
		Without weighting		Capacity weighting		Area weighting	
		mean	sd	mean	sd	mean	sd
$r_B = \infty$, $p = 0.059$	78%	1.73	0.25	1.71	0.24	1.73	0.25
$r_B = 30$, $p = 0.081$	78%	1.66	0.16	1.64	0.16	1.65	0.16
$r_B = 18$, $p = 0.116$	78%	1.64	0.15	1.63	0.15	1.65	0.16
$r_B = 6$, $p = 0.555$	78%	1.62	0.14	1.61	0.14	1.62	0.14
3D X-ray image	78%	1.51	0.16	1.51	0.16	1.51	0.16

Table 2: Mean values and standard deviations of tortuosity characteristics

Used data	Porosity	Pore size		Coordination number		relative length of MST
		mean	sd	mean	sd	mean
$r_B = \infty$, $p = 0.059$	78%	10.16	4.38	4.37	2.01	0.46
$r_B = 30$, $p = 0.081$	78%	10.11	4.36	4.36	2.00	0.47
$r_B = 18$, $p = 0.116$	78%	10.13	4.36	4.36	1.99	0.47
$r_B = 6$, $p = 0.555$	78%	10.12	4.37	4.34	1.97	0.47
3D X-ray image	78%	8.05	3.74	4.38	5.31	0.44

Table 3: Mean values and standard deviations of pore size and coordination number; mean relative length of MST

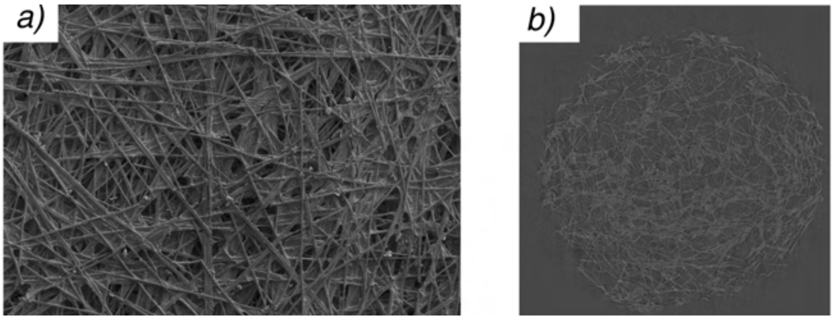

Figure 1: Visualization of a gas diffusion layer – manufacturer: Toray: (a) 2D SEM image of a GDL; (b) Thin–section of a 3D image of a GDL

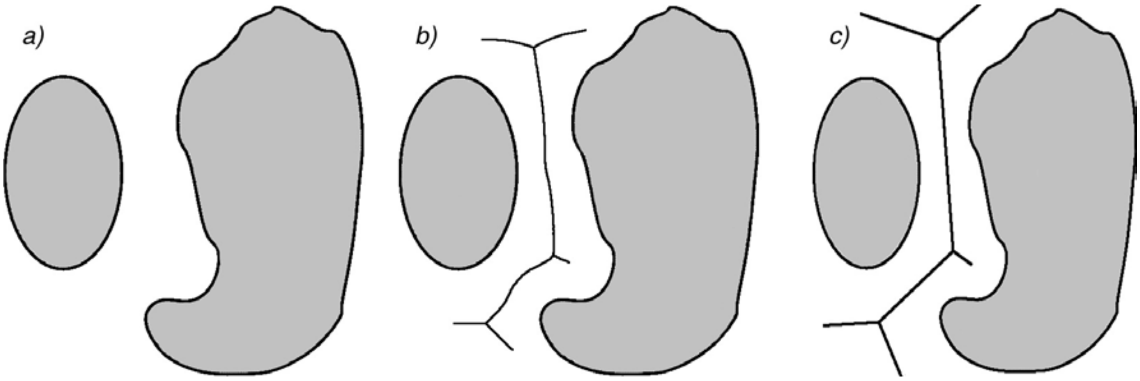

Figure 2: Skeletonization and transformation into vector data of the empty space – 2D example: (a) Considered objects with empty space; (b) Skeletonized empty space; (c) Transformed skeletonization results into vector data

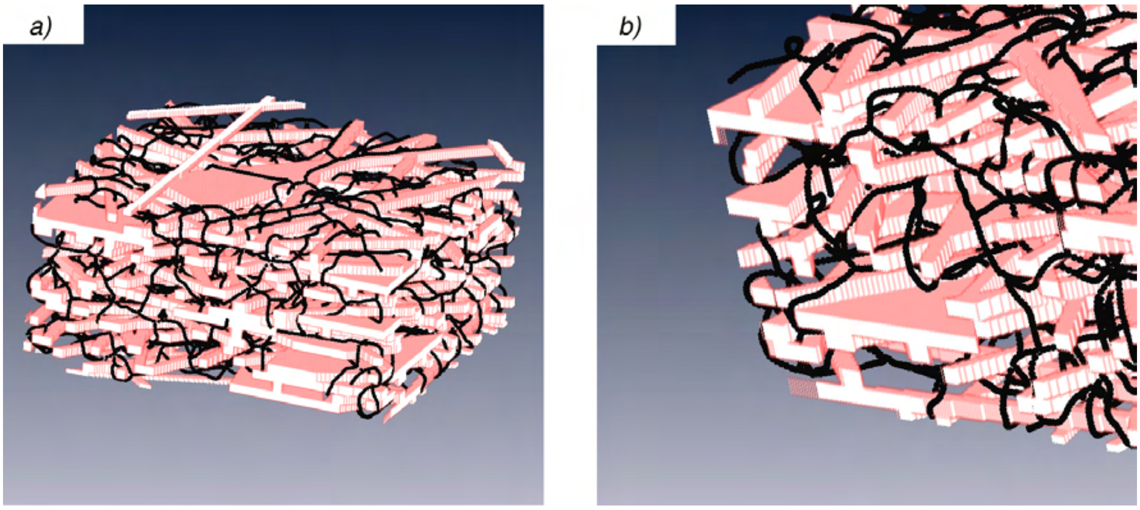

Figure 3: Results of the 3D skeletonization of the pore space: (a) Multi–layer model with skeletonized pore space; (b) Magnification

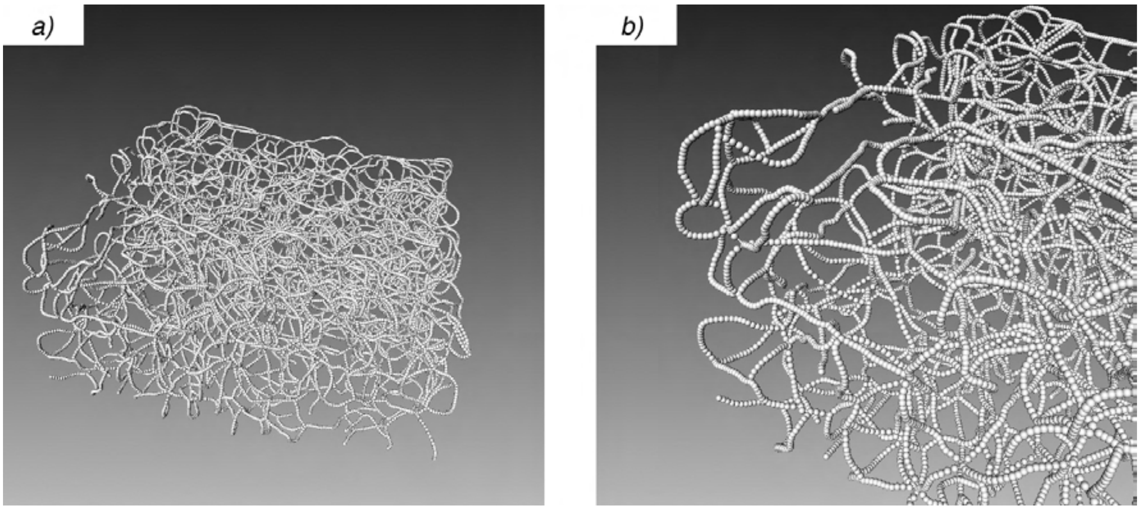

Figure 4: Graph representation of the pore space: (a) 3D skeleton of the pore space; (b) Magnification

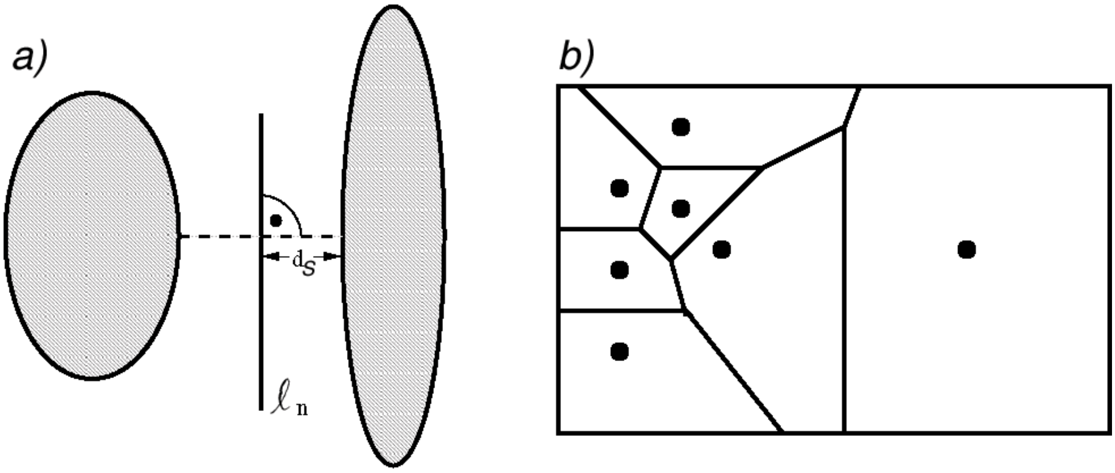

Figure 5: Weights of the shortest paths: (a) 2D example of the shortest distance d_S of a segment ℓ_n to the solid phase (b) Schematic display of area weights

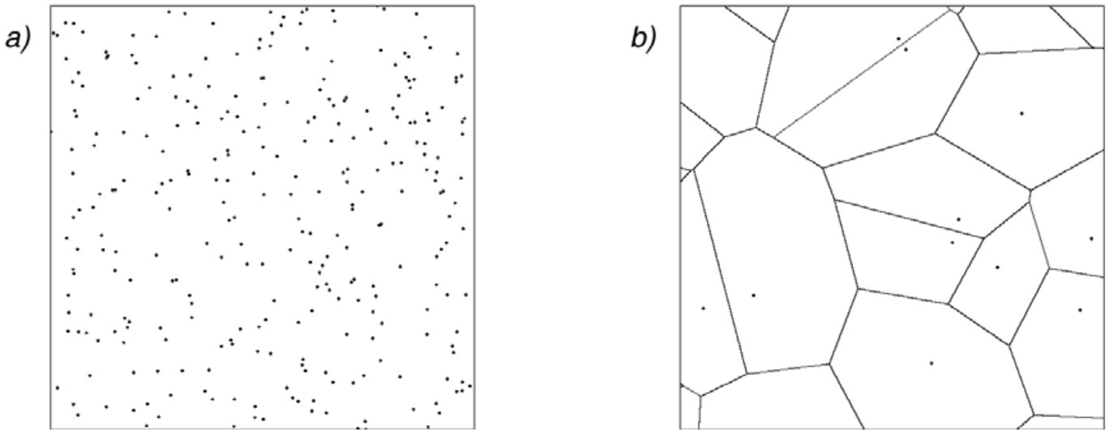

Figure 6: Stochastic geometry models: (a) Realization of a Poisson point process; (b) Realization of a Poisson–Voronoi tessellation with nuclei (magnification)

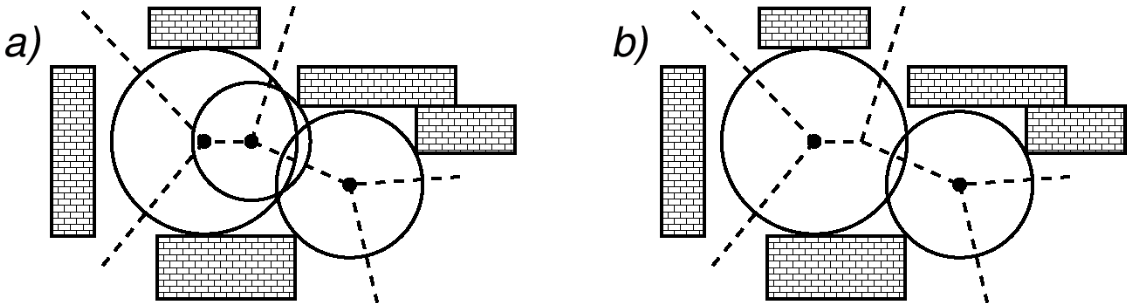

Figure 7: Pore center: (a) A graph with all potential pores (the balls around each vertex); (b) The considered pores

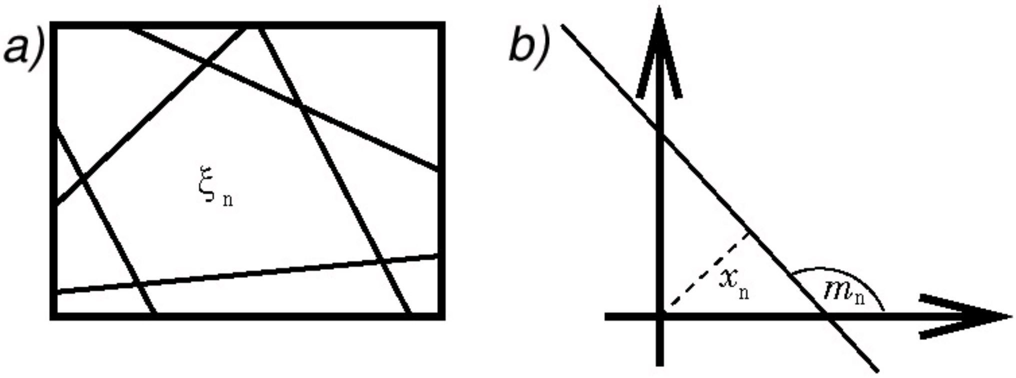

Figure 8: Line tessellations: (a) Cell ξ_n of a planar line tessellation; (b) Normal form of a line in $\mathbb{R}^2$

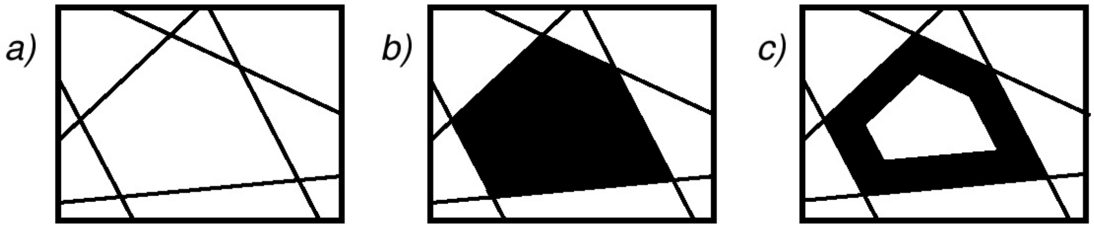

Figure 9: Binder modeling: (a) PLT; (b) Binder modeled by Bernoulli filling (c) Binder modeled by dilation

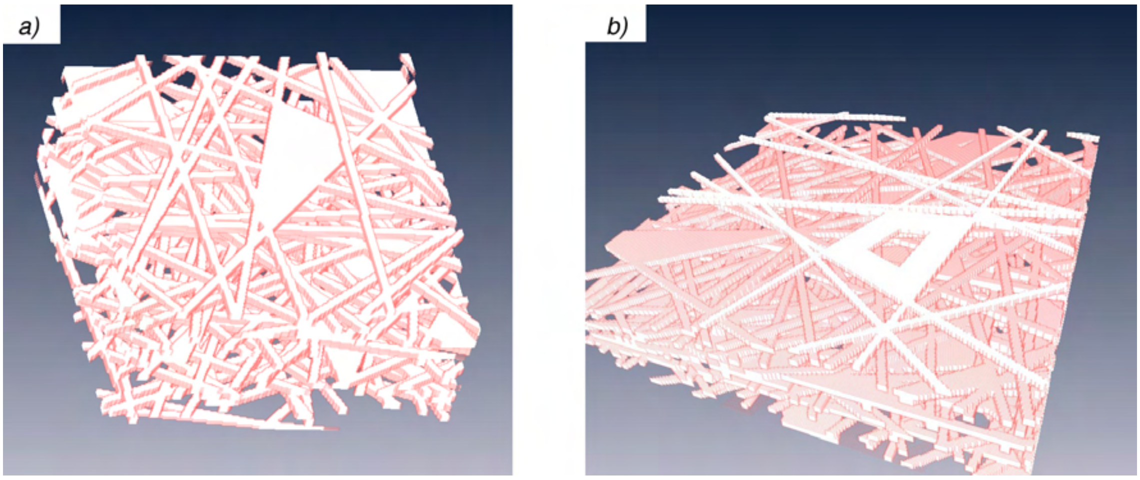

Figure 10: Realizations of the 3D multi–layer model: (a) Binder is modeled by a complete cell filling; (b) Binder is modeled by a partial cell filling

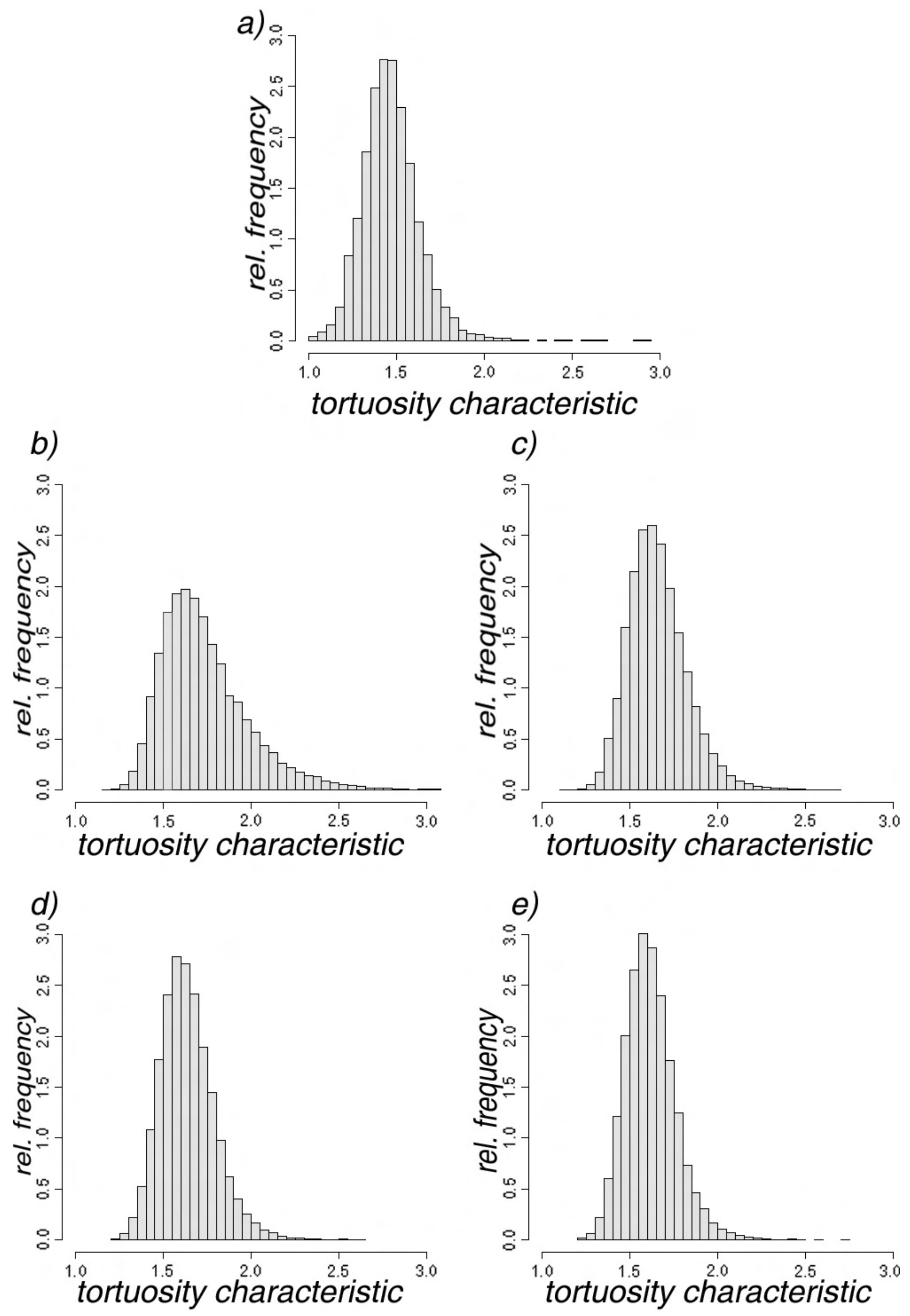

Figure 11: Tortuosity characteristic without weighting: (a) Real 3D data set; (b) Complete cell filling; (c) Partial cell filling with $r_B = 30$; (d) Partial cell filling with $r_B = 18$; (e) Partial cell filling with $r_B = 6$

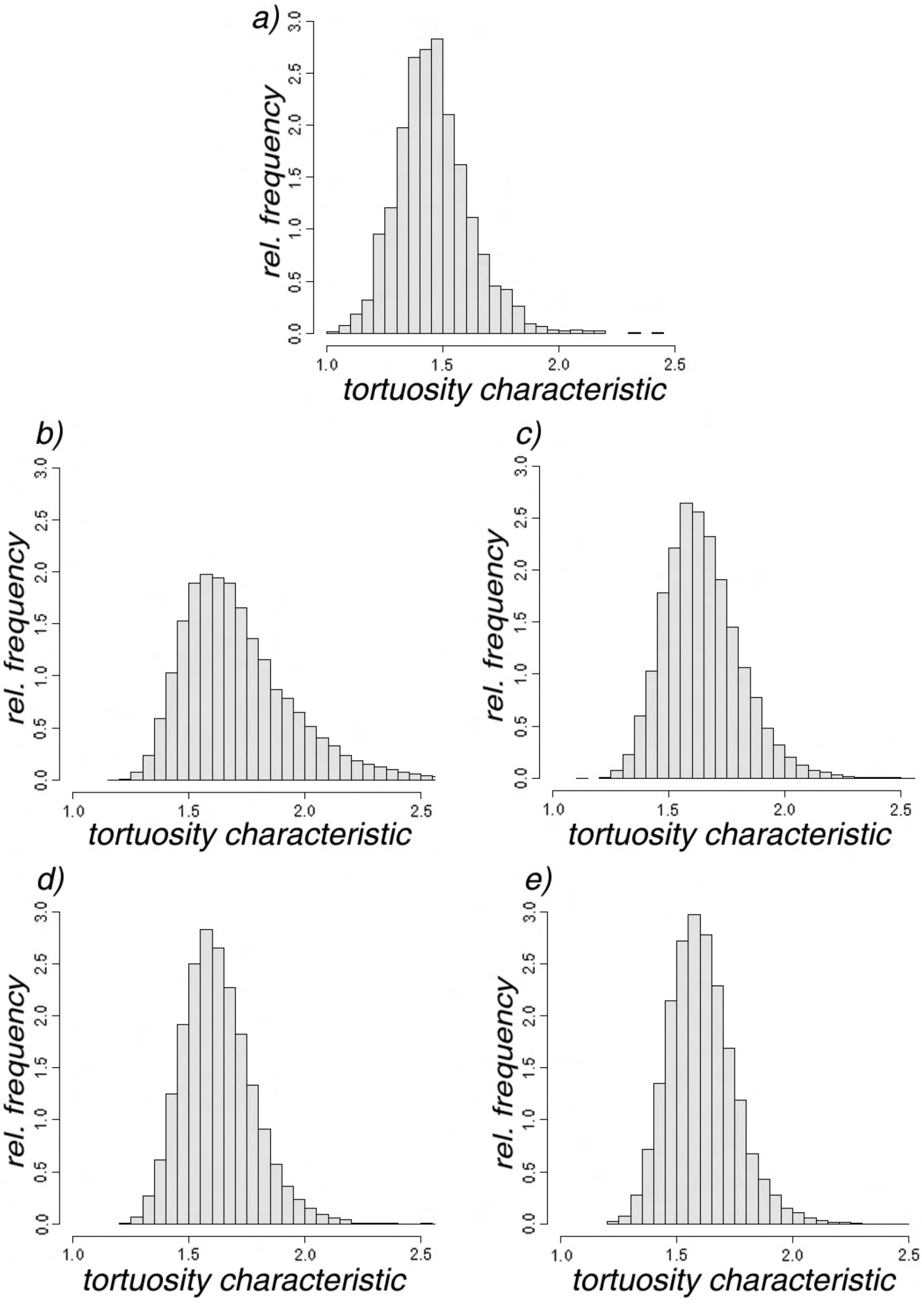

Figure 12: Capacity–weighted tortuosity characteristic: (a) Real 3D data set; (b) Complete cell filling; (c) Partial cell filling with $r_B = 30$; (d) Partial cell filling with $r_B = 18$; (e) Partial cell filling with $r_B = 6$

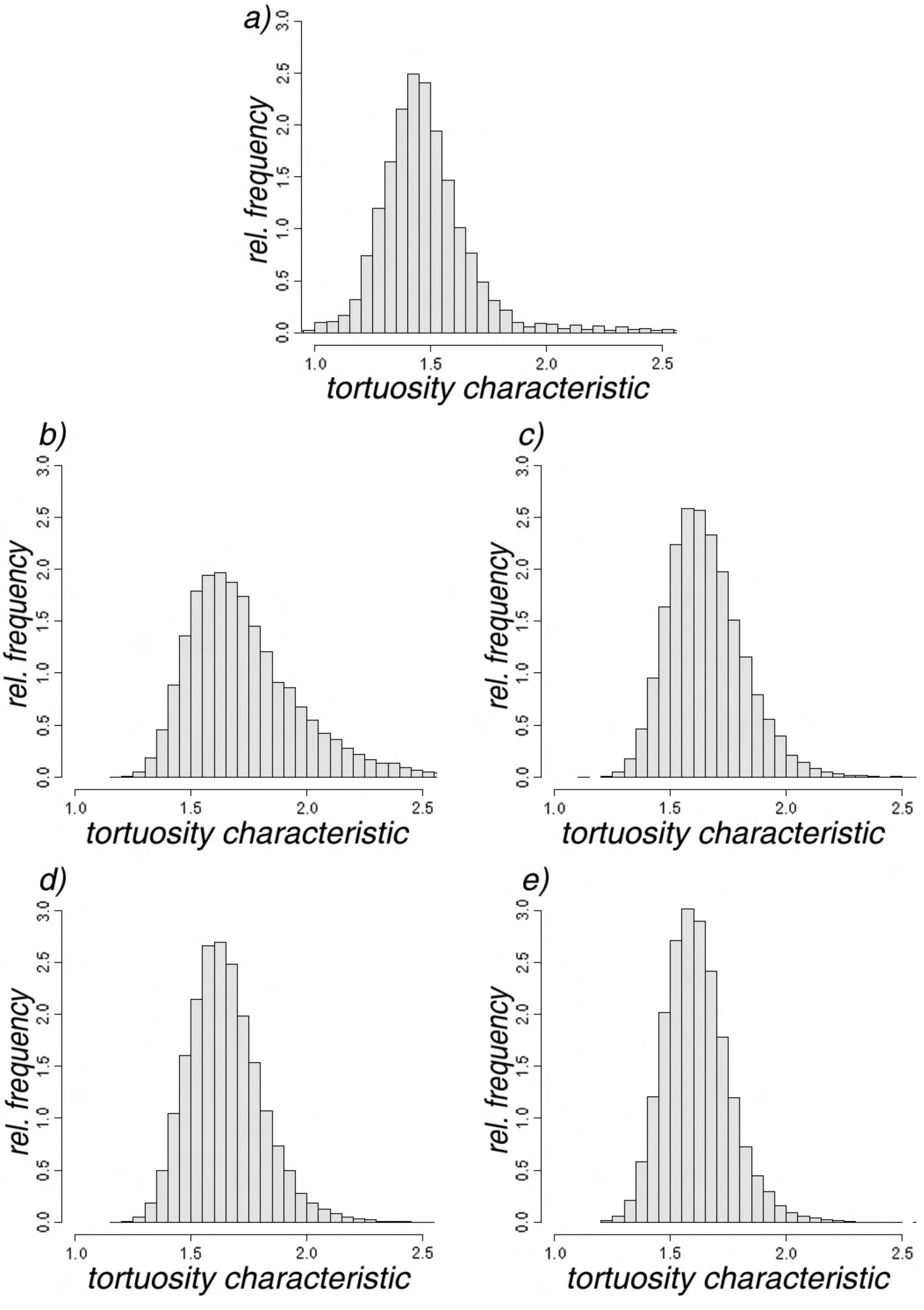

Figure 13: Area–weighted tortuosity characteristic: (a) Real 3D data set; (b) Complete cell filling; (c) Partial cell filling with $r_B = 30$; (d) Partial cell filling with $r_B = 18$; (e) Partial cell filling with $r_B = 6$

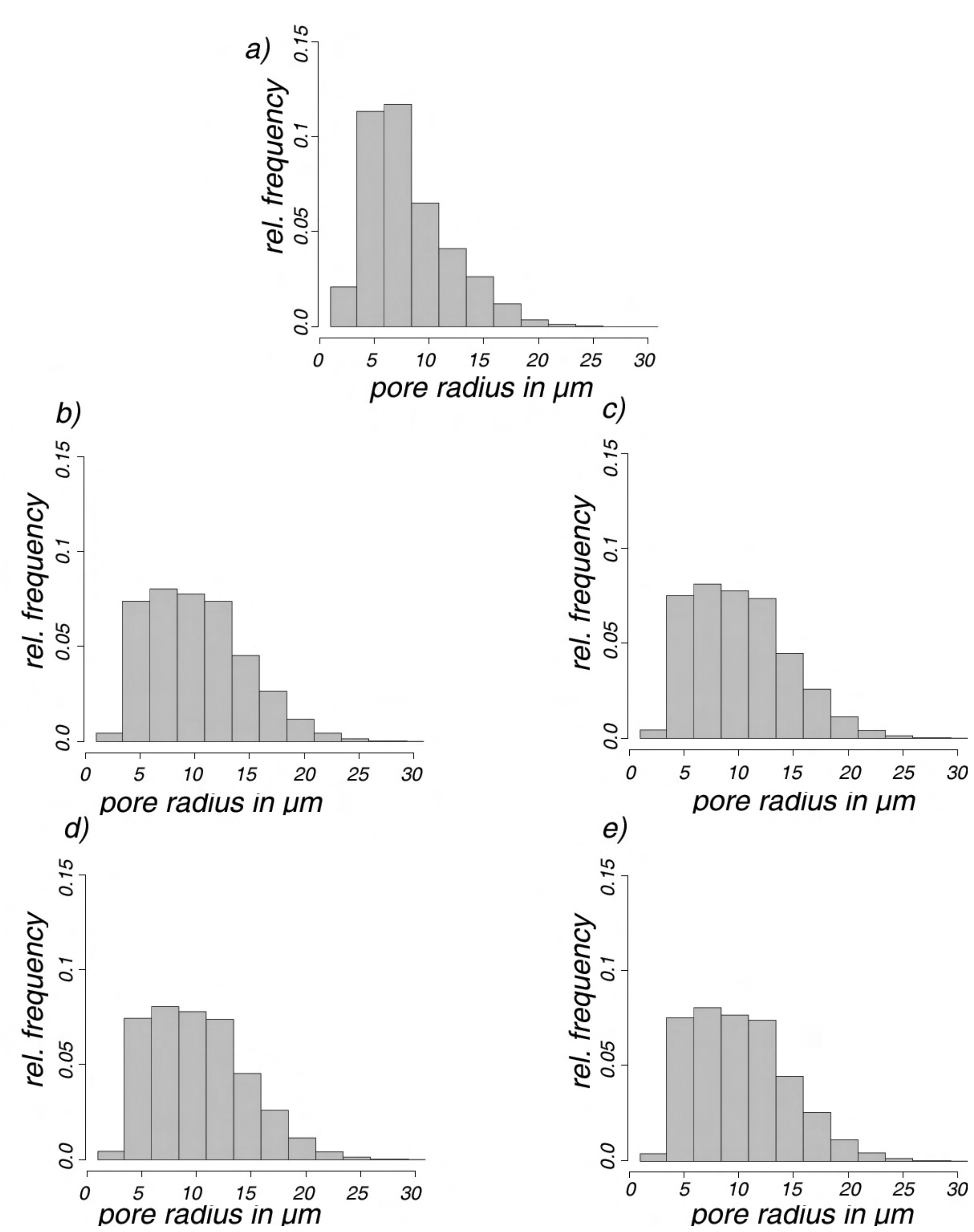

Figure 14: Pore size distribution: (a) Real 3D data set; (b) Complete cell filling; (c) Partial cell filling with $r_B = 30$; (d) Partial cell filling with $r_B = 18$; (e) Partial cell filling with $r_B = 6$

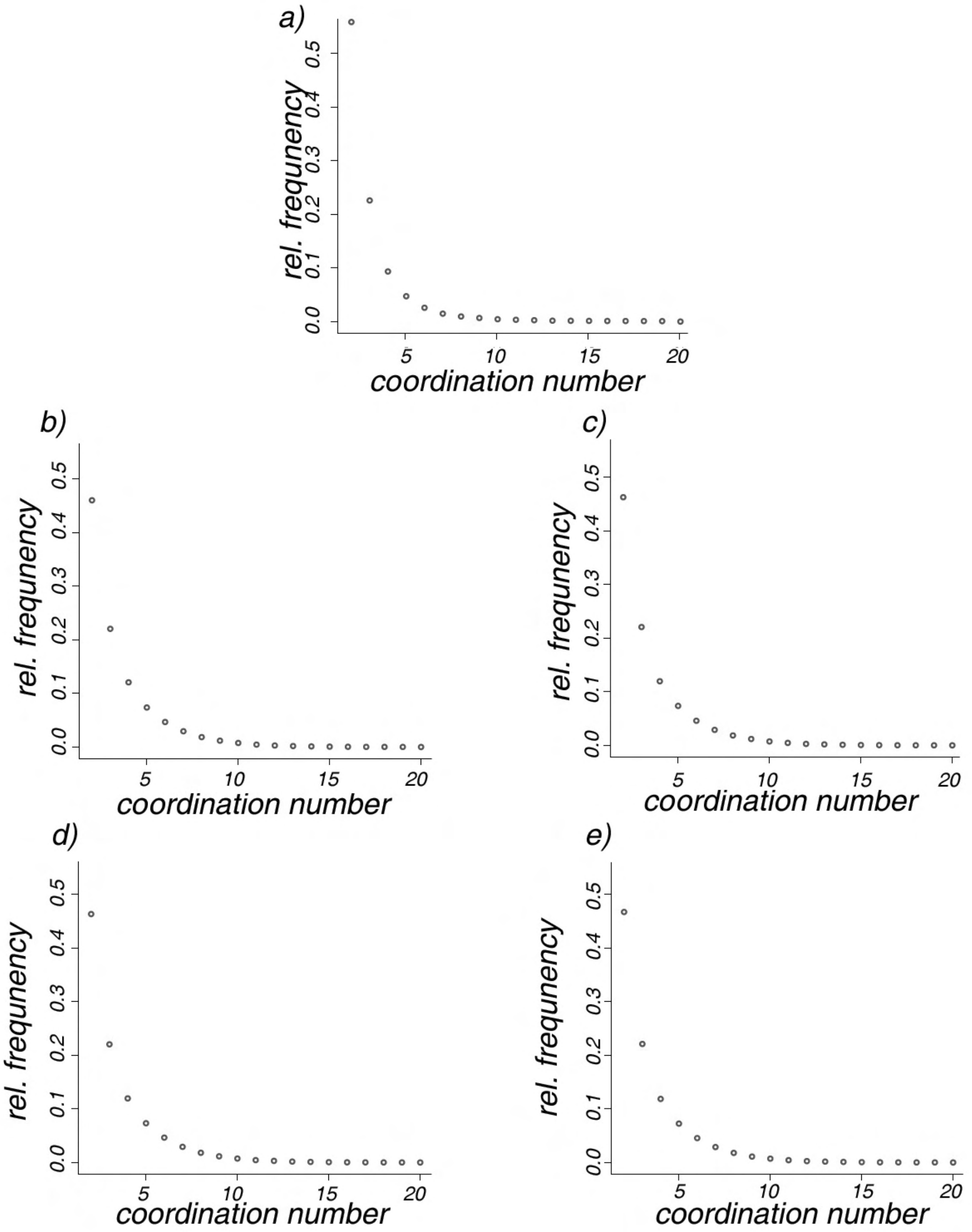

Figure 15: Coordination number: (a) Real 3D data set; (b) Complete cell filling; (c) Partial cell filling with $r_B = 30$; (d) Partial cell filling with $r_B = 18$; (e) Partial cell filling with $r_B = 6$